ELSEVIER

Magnetic Resonance Imaging 22 (2004) 529–542

MAGNETIC RESONANCE IMAGING

A novel phantom and method for comprehensive 3-dimensional measurement and correction of geometric distortion in magnetic resonance imaging

Deming Wang*, David M. Doddrell, Gary Cowin

Centre for Magnetic Resonance, The University of Queensland, Brisbane 4072, Australia

Received 15 June 2003; accepted 23 January 2004

Abstract

A phantom that can be used for mapping geometric distortion in magnetic resonance imaging (MRI) is described. This phantom provides an array of densely distributed control points in three-dimensional (3D) space. These points form the basis of a comprehensive measurement method to correct for geometric distortion in MR images arising principally from gradient field non-linearity and magnet field inhomogeneity. The phantom was designed based on the concept that a point in space can be defined using three orthogonal planes. This novel design approach allows for as many control points as desired. Employing this novel design, a highly accurate method has been developed that enables the positions of the control points to be measured to sub-voxel accuracy. The phantom described in this paper was constructed to fit into a body coil of a MRI scanner, (external dimensions of the phantom were: 310 mm × 310 mm × 310 mm), and it contained 10,830 control points. With this phantom, the mean errors in the measured coordinates of the control points were on the order of 0.1 mm or less, which were less than one tenth of the voxel's dimensions of the phantom image. The calculated three-dimensional distortion map, i.e., the differences between the image positions and true positions of the control points, can then be used to compensate for geometric distortion for a full image restoration. It is anticipated that this novel method will have an impact on the applicability of MRI in both clinical and research settings, especially in areas where geometric accuracy is highly required, such as in MR neuro-imaging.

Keywords: Geometric distortion; 3-Dimensional phantom; Comprehensive assessment; Full restoration; Magnetic resonance imaging

1. Introduction

Magnetic resonance imaging (MRI) has revolutionized diagnostic imaging for the past two decades. This imaging modality can explore the physical properties of tissue with great details and is probably the most powerful imaging technique in the current practice of radiology, especially for imaging of the brain. In recent years there has been an explosion of research activities in brain research using structural and functional MRI. In fact, MRI has become the most valuable radiological technique for both structural and functional study of the brain. In general, MRI is now being widely used in nearly every aspect of radiological examinations and it is gradually replacing other imaging modalities, becoming the favored modality of choice.

Magnetic resonance imaging does have some limitations: its constraints are related to the homogeneity of the field generating devices used to form the image. Geometric distortion arising from magnetic field inhomogeneity and gradient field non-linearity has been one of the major concerns. The current generation of MRI scanners has been designed with gradient rise times of less than 200 μs. In order to achieve such short rise times, gradient designers have restricted the length of the gradient coils and also used fewer turns. Such restrictions have led to an increase in the gradient field non-linearity, the result being image distortions. Although slight distortions in MR images normally have little consequences in routine radiological examinations, geometric distortion can be a serious problem in certain MRI applications where high geometric accuracy is required. Examples where precision is a primary consideration include image-guided surgery and volumetric quantification.

Geometric distortion arising from the static field inho-

* Corresponding author. Tel.: +61-7-33654100; fax: +61-7-33653833.

E-mail address: deming@cmr.uq.edu.au (D. Wang).

0730-725X/04/$ – see front matter
doi:10.1016/j.mri.2004.01.008

mogeneity and gradient field non-linearity has been studied by specially designed phantoms [1–12]. Nearly all of these phantoms, however, were designed for 2D (two-dimensional) measurements. Two major design approaches have been employed; one uses square grids [1–3] and the other uses cylindrical rods [4–6] or capillary tubes [7]. A common feature in both design approaches is that the control points are defined only through the intersection of the imaging plane with the grids or cylindrical rods. A clear limitation in these approaches is that only the two coordinates of the control points' locations in the imaging plane can be measured. The third coordinate that is perpendicular to the imaging plane is immeasurable and is unknown. Therefore, the measurement of geometric distortion with 2D phantoms provides only an incomplete description of the image distortion. Apart from this serious limitation, to map geometric distortion in the entire imaging volume using 2D phantoms is time-consuming. It often requires measurements with the phantom positioned at different locations and with different orientations. Additional errors can easily be introduced in the process of repositioning.

For a complete mapping of geometric distortion in MRI, control points defined in three dimensions (3D) are required. To the authors' knowledge, there has been only one study that used control points defined in 3D [11,12]. To study geometric distortion in MRI, Breeuwer et al. used spheres of a certain size arranged in three dimensions [11]. Two slightly different design approaches were developed. In order to specify the positions of the control points, the centre of the gravity of the spheres was used to generate the control points' positions. To ensure accuracy, such an approach requires the spheres employed to have a sufficient size. In their design, spheres of 11 mm in diameter were used [11]. This requirement puts a limit on the number of spheres that can be arranged in a phantom. These authors described the construction of two phantoms that contained 427 and 793 control points, respectively [11]. In their analysis, the accuracy associated with the positional measurement of the control points appeared to be dependent on a number of factors, including the size of the image voxels.

For a comprehensive and accurate mapping of geometric distortion in 3D, two key requirements are fundamental. First, the number of sampling points (control points) needs to be sufficiently large in order to provide a comprehensive mapping of the spatial variations of the distortion. Dense sampling is necessary if detailed spatial information on local deformations is to be obtained. Secondly, the accuracy with which the positions of these sampling points are measured is vitally important, and this accuracy in fact ultimately determines the spatial quantification of the geometric distortion. The two goals that are the key requirements of the 3D phantom proposed in this article are to acquire a sufficiently large number of control points and a method that can accurately measure the positions of the control points.

The article is organized as follows. In section 2, the design of the 3D phantom is described. This is followed by the development of a method that has been specifically implemented to measure the positions of the control points in the MR images of the phantom. Then, a procedure for geometric distortion correction using the measured distortion maps is outlined in section 4. Reproducibility and accuracy assessments of the method are discussed in section 5 and the results are presented in section 6. The final two sections (7 and 8) are included outlining the merits of the method and the potential impact it may bring on MRI in general and on MR neuro-imaging in particular.

2. The 3D phantom

Conceptually, there are only two simple ways that can be used to define a point in space. Either the "point-like" objects that can be "distinguished" in the image are used, or a set of three orthogonal planes are employed and their intercepting point can be used to define a point in space. The approach of using "point-like" objects, i.e., spheres, has been explored by Breeuwer et al. [11]. As acknowledged by these investigators, this approach has limitations, particularly on the number of control points that can be introduced. It is important to develop an alternative method.

The central idea used in the design of the 3D phantom proposed to address the issues outlined above is illustrated in Fig. 1. As indicated by the arrows, each cross on the surface of the grid sheet can be used to define a point in space. These points can be viewed as the intercepting points of the three orthogonal planes: the two planes that define the crosses and the plane of the sheet surface. These well-defined intersections at the surface of the grid sheets in 3D are used as the control points in the approach described herein.

A photograph of the 3D phantom that was constructed to fit into a body coil based on this design is shown in Fig. 2. The phantom has a very simple structure. It consists simply of layers of grid sheets aligned in parallel with equal spacing along the third dimension (the z axis) to create a 3D array of points. The spacing between the sheets is the same as the width of the sheet, so the control points along the z axis are also equally spaced. The external dimensions of the phantom are 310 mm $\times$ 310 mm $\times$ 310 mm, which forms a cube. The wall materials used are 10.00 mm Perspex sheets. The core materials of the phantom are the plastic grid sheets. These grid sheets are normally used for building ventilation and were purchased commercially. All the wall plates and the plates of the grid sheets used for the construction of the phantom were machined with precision to ensure the regularity of the grid pattern of the phantom. The grids are slightly non-square, 14.28 mm along one dimension (denoted as the x direction) and 14.39 mm along the other dimension (denoted as the y axis). The width of the grid sheets is 9.0 mm.

In the phantom shown in Fig. 2, the grid sheets contained

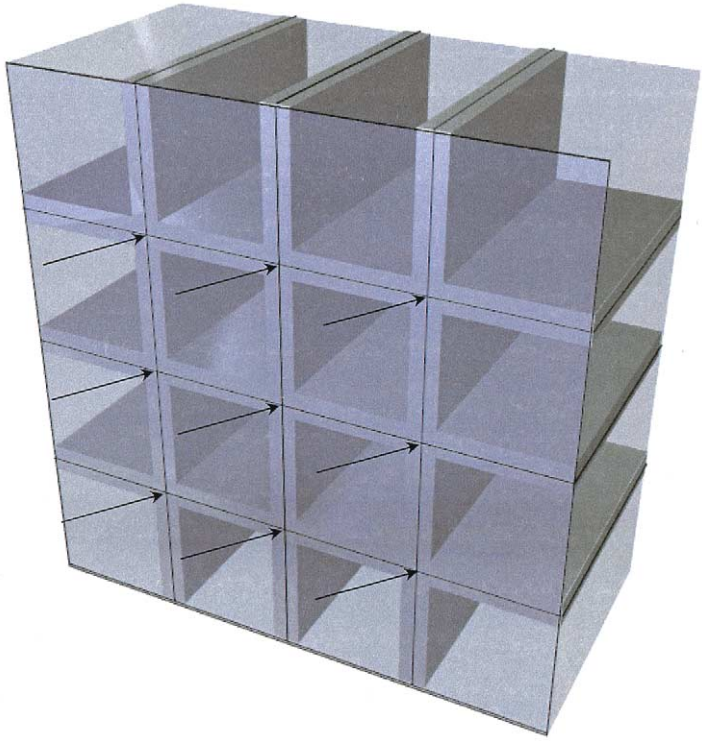

Fig. 1. A schematic illustration of the control points (indicated by the arrows) generated using three orthogonal planes.

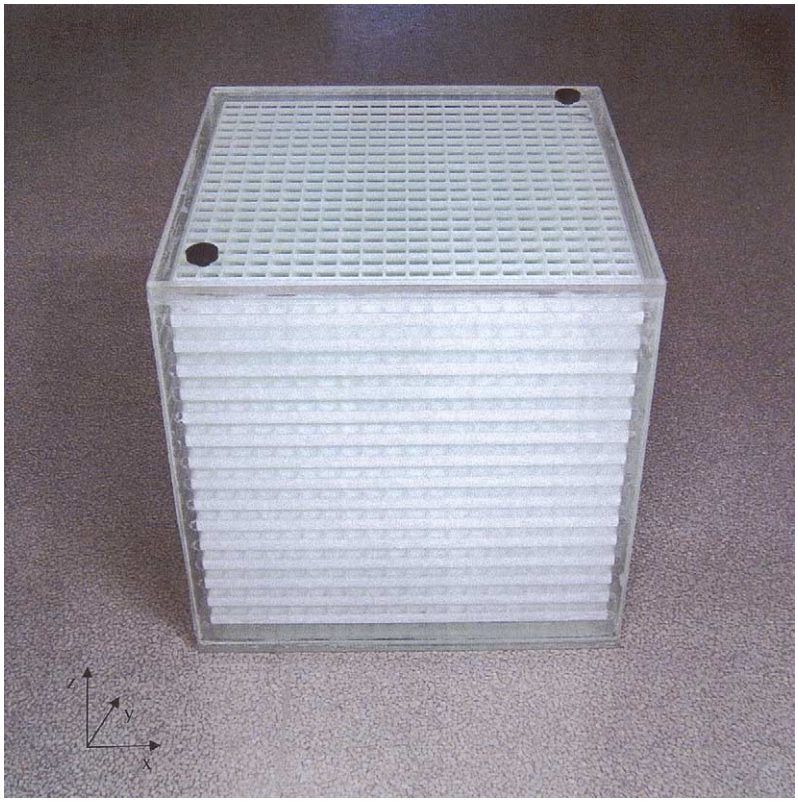

Fig. 2. A photograph of the 3D phantom. The coordinate axis system used in relating to the orientation of the phantom is shown in the bottom left corner.

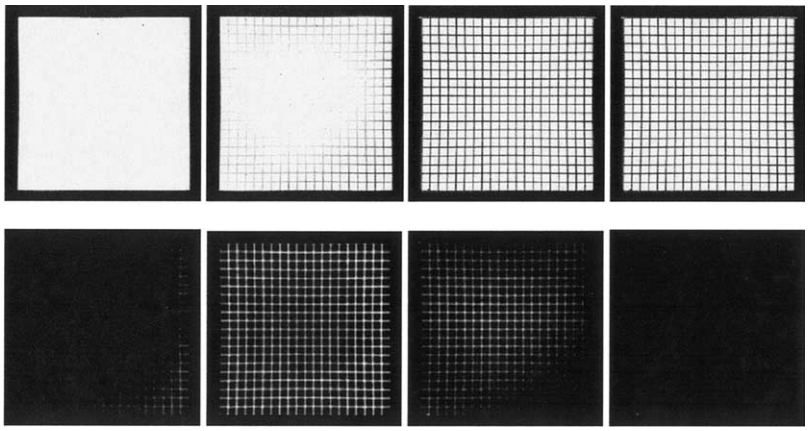

Fig. 3. A sequence of transverse slices selected in close proximity to an interface between a grid sheet surface and surrounding water (top row); and the corresponding images based on the magnitude of the first derivative calculated along the z axis using a 3D Prewitt operator (bottom row).

19 grid crosses along the x and y axes, producing $19 \times 19 = 381$ points on each side of the sheet surfaces. The phantom contained 15 grid sheets. Therefore, there are a total of 10,830 ($19 \times 19 \times 30$) points that can be used as control points. These points form a regular 3D array. The dimensions between the array points along the three orthogonal axes are denoted, respectively, as C_x, C_y and C_z. For the phantom shown in Fig. 2, $C_x = 14.28$ mm, $C_y = 14.39$ mm and $C_z = 9.00$ mm. To complete the phantom, the water solution that filled the phantom was prepared according to the method recommended by AAPM (American Association of Physicists in Medicine) [1].

3. The measurement of the positions of the control points

A distinctive feature of the proposed method lies in the manner in which the positions of the control points are measured. The positions of the control points are determined by the positions of the planes (see Fig. 1). Specifically, the z coordinate is determined by the interfacial boundary formed between the surface of the grid sheet and the water; the x and y coordinates are each determined by a pair of interfaces between the grid side walls and the water, with the middle position of the two interfaces taken as the x and y coordinates. Therefore, in the present method the measurement of the positions of the control points becomes the measurement of the positions of the interfacial boundaries. These interfacial boundaries are normally manifested as image edges and the extraction of the interfacial boundaries becomes a problem of edge detection. There is extensive literature on image edge detection, particularly for 2D images. The method described herein employs the first derivatives evaluated in three dimensions to detect these edges and consequently to detect the interfacial boundaries. The operators used for deriving approximate first derivatives in three dimensions are the extended 3D Prewitt operators that are described in Appendix A.

The method that has been specifically developed for the measurement of the positions of the control points in the MR images of the 3D phantom described in this article is fully automated. This novel method involves two separate steps. The first step is to identify a set of reference voxels whose positions can be taken as an initial estimation for the positions of the control points in the image. In conventional approaches using point-like objects as source of control points, clusters of voxels whose center of gravity is taken as an approximation for the positions of the control points have been used. In the present approach, wherein orthogonal planes are employed to define the control points, a different method has been developed. This method will be presented in the following subsection and will provide an initial estimate for the positions of the control points. The final positions of the control points in the present method are determined by the positions of the planes. The measurement of the positions of the planes uses the first moments calculated on the images formed by the magnitude of the first derivatives. This is done in a subsequent step. The initial position of the control points estimated in the first step is used to assist an optimal placement of a region of interest in which the positions of the planes are to be evaluated. The two steps are described separately below.

3.1. Identification of the reference voxels for initial estimation for the positions of the control points

As noted, the interfacial boundaries that are used to define the control points in the present method are manifested as image edges, and this is demonstrated in Fig. 3. In Fig. 3, the top row shows a sequence of transverse slices of the gray scale intensity images in proximity to an interfacial boundary between a grid sheet surface and the water. Moving from left to right, the slice's position moves from a position in the gap (the water) near the interface to a position that cuts through the grid sheet. As shown, the interfacial boundary occurred near the slice second from the left. In the bottom row, the images based on the magnitude of the

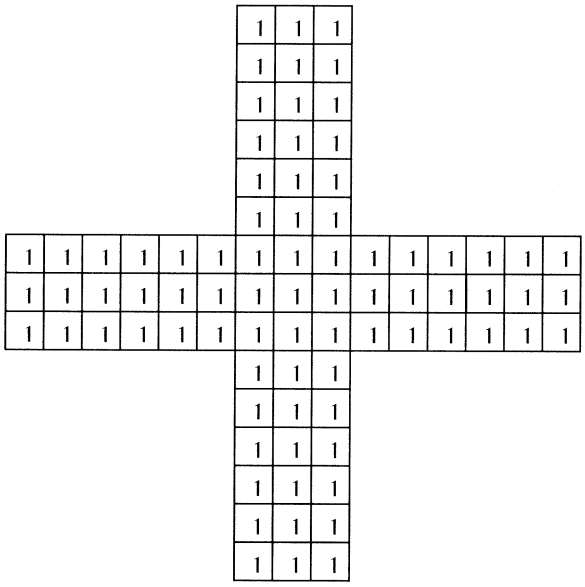

Fig. 4. A 2D mask used in a convolution for enhancement of the prominence of the voxels at the crosses in the derivative images.

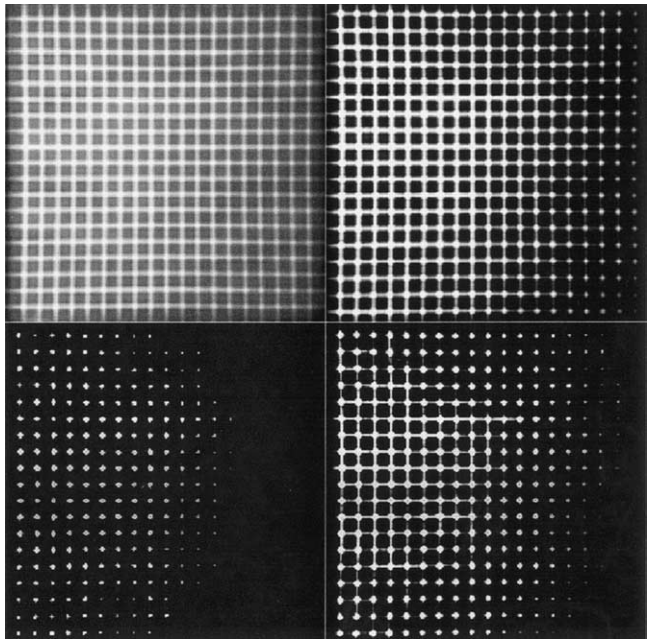

Fig. 5. A representative transverse slice of the convoluted derivative image (top left corner) and three images obtained with different threshold levels to aid visual recognition of the enhanced prominence of the voxels at the crosses.

first derivative along the z axis, $|g^z(i, j, k)|$, Eq. (A4), are shown. It is clearly demonstrated here that the interfacial boundary is manifested as image edges.

The next step is to further enhance the prominence of the voxels at the crosses comparatively to those on the edges of the grids, as only the voxels at the crosses are the potential candidates for the reference voxels. This is achieved through a convolution using a cross-like mask as shown in Fig. 4. The convolution of this mask with $|g^z(i, j, k)|$ will clearly add more intensity weight for voxels at the crosses than those on the edges of the grids. The size of the mask used in this convolution is not particularly crucial and the one shown in Fig. 4 was one of a number of masks that were investigated. The convolution was carried out in the xy plane. A representative transverse slice of the convoluted derivative image is shown in Fig. 5 (the top left corner; and the three images included in the figure that were obtained with different threshold levels were to make the prominence of the crosses more perceptible). In Fig. 6, two representative 1D intensity profiles, one selected along the x axis (a) and the other selected along the y axis (b), are presented. As clearly shown here, the intensity of the voxels at the crosses is significantly higher. The 19 peaks in each profile correspond to the 19 crosses. In the method, these voxels are used as the reference voxels that are to provide an initial estimation for the positions of the control points.

3.2. The final measurement of the positions of the control points by using the positions of the planes

The identified reference voxels provide an initial estimation of the position of the control points in the phantom images and are used to assist in the calculation of the positions of the planes from which the positions of the control points are finally determined. The positions of the three planes are determined using the first moments of the magnitude of the first derivatives evaluated along the three principal axes [Eqs. (A2)–(A4)]. In order to gain insight into the calculation of the positions of the planes, it is useful to examine some ID profiles of image gray scale intensity and the magnitude of the first derivatives in the neighborhood of a control point.

In Fig. 7a, representative 1D profiles of the image intensity for a group of voxels sequentially selected along a line parallel to the z axis near two control points are shown, and in Fig. 7b, the profiles of the magnitude of the first derivative for the selected voxels calculated along the z direction are given. As shown, the z positions of the planes (the interfacial boundary between the surface of the grid sheet and the water) are well defined, especially in the derivative profiles in Fig. 7b. In the method, the z position of the planes is defined as the central position of the peak in the derivative profile. These central positions can be measured using the first moment $\bar{K}(i, j)$

$$\bar{K}(i,j) = \frac{\sum_{p=1}^{n_z} k_p |g^z(i,j,k_p)|}{\sum_{p=1}^{n_z} |g^z(i,j,k_p)|} \tag{1}$$

where n_z is the number of voxels used in the evaluation of the first moment. Typical values for n_z are 5, 7 or 9. The position $[i, j, \bar{K}(i, j)]$ is then taken as the position of the plane at the sampled location. In the method, the plane is sampled

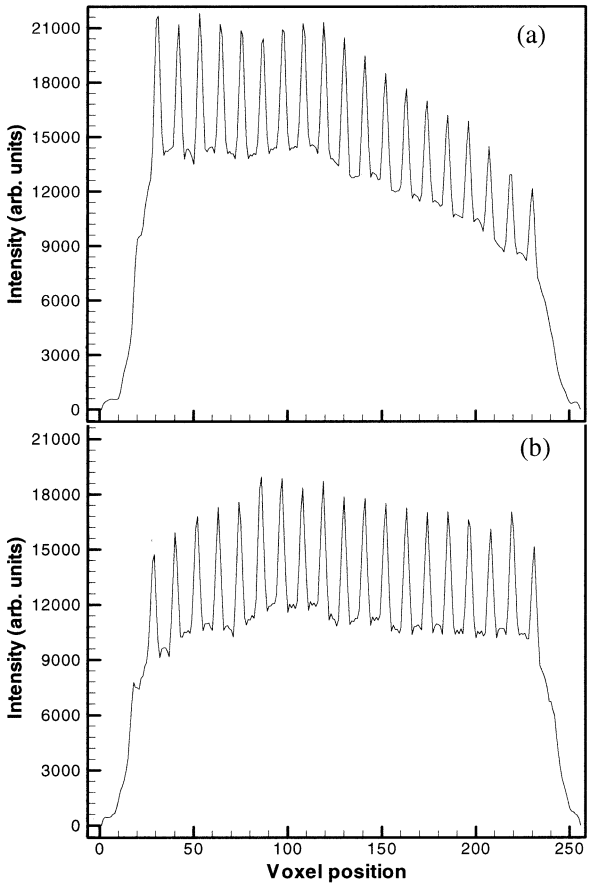

Fig. 6. (a) and (b) illustrate two representative 1D intensity profiles, one selected along the x axis (a) and one selected along the y axis (b) of the convoluted derivative images. The two lines were selected passing at the central cross (see Fig. 5).

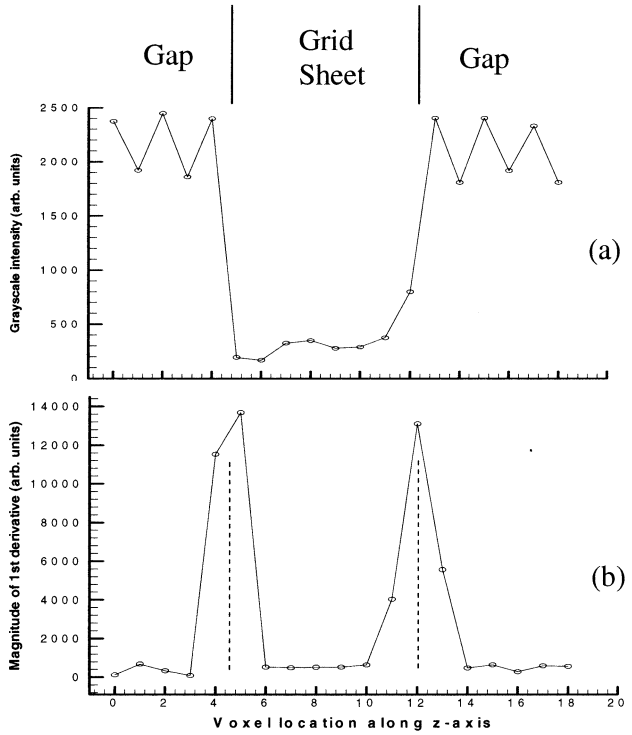

Fig. 7. (a) and (b) illustrate representative 1D profiles of the image intensity for a sequence of voxels taken along a line parallel to the z axis (a); and the magnitude of the first derivative calculated along the z axis for the same voxels (b). The two edges in (a) correspond to the two interfacial boundaries between the grid sheet surfaces and the water. The dashed lines in (b) indicate the positions of the interfacial boundaries and were obtained using the first moments.

in a small neighborhood. For the plane perpendicular to the z axis, a neighborhood of 3×3 or 5×5 is used. These sampled plane positions can be fitted into a plane equation in 3D using an algorithm such as the non-linear Levenberg-Marquardt method. The plane obtained by such a non-linear fitting method, together with the other two planes to be derived in a similar manner from the first derivatives calculated along the x and y axes, will yield an intercepting point and this point could be taken as a control point. However, in a fully automated algorithm such as the one presented herein, the use of a fitting process may pose problems in implementing an effective procedure for convergence checks. Therefore, in the method an approximation was used. In this approximation, the mean value of the sampled $\bar{K}(i, j)$ in the specified neighborhood is taken as the z coordinate of the control point. In a similar fashion, the x and y coordinates are assigned by the mean positions of the other two planes to be described in the next paragraph. In fact, the voxels used in the determination of the position of the plane form a volume and this volume is referred to as plane sampling volume (PSV). For the determination of the z position of the control points, this volume is denoted as PSV(z). For a neighborhood of 5×5 with 7 voxels used in the evaluation of the first moment, PSV(z) is $5 \times 5 \times 7$. The placement of the PSV(z) is centred at the reference voxels.

The measurements of the positions of the control points along the x and y axes are carried out in a very similar manner to that for the z coordinate. In Fig. 8a, representative 1D profiles of the image intensity for voxels sequentially selected along a line parallel to the x axis near two control points are shown, while in Fig 8b the magnitude of the first derivative calculated along the x axis for the same voxels is given. As shown in Fig. 1, for the x (and y) coordinate, two interfacial boundaries on the both sides of the grid wall are employed. As the separation between the two boundaries is the width of the grid wall, which is only ~1.5 mm, the two interfacial boundaries are very close, as indicated as slopes in the intensity profile (a) and peaks in the derivative profile (b). The middle position between the two interfacial boundaries will be taken as the x position of the plane perpendicular to the x axis. These middle positions can be approximated by the first moment $\bar{I}(j, k)$

$$I(j,k) = \frac{\sum_{p=1}^{n_x} i_p |g^x(i_p, j, k)|}{\sum_{p=1}^{n_x} |g^x(i_p, j, k)|} \tag{2}$$

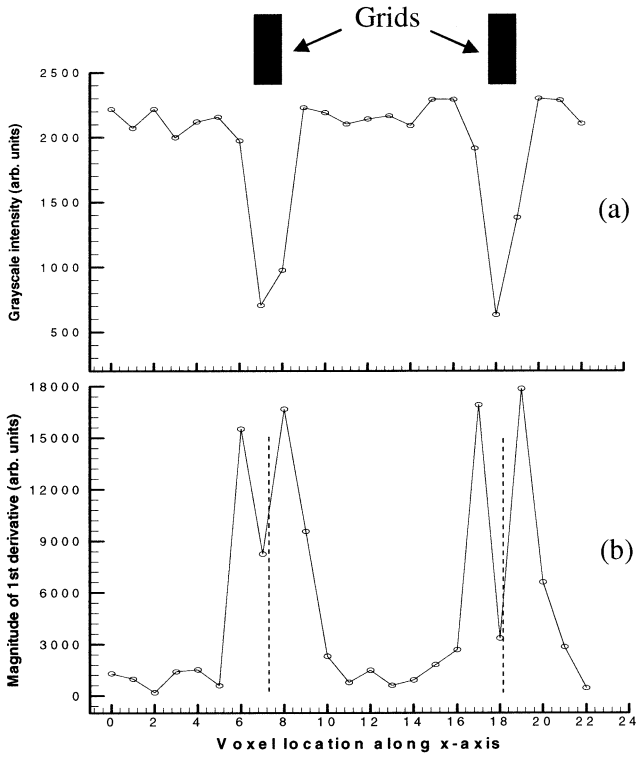

Fig. 8. (a) Representative 1D profiles of the image intensity for a sequence of voxels taken along a line parallel to the x axis; (b) The magnitude of the first derivative calculated along the x axis for the same voxels. The two close interfacial boundaries between grid sidewalls and the water are well resolved in the derivative profile (b). The dashed lines in (b) indicate the middle positions of the interfacial boundaries and were obtained using the first moments.

where n_x is the number of voxels used in the evaluation of the first moment and $|g^x(i, j, k)|$ is the magnitude of the first derivative along the x axis [see Eq. (A2)]. Typical values for n_x are 7, 9 or 11. The dashed lines in Fig. 8b indicate the middle positions of the interfacial boundaries determined by the first moment, $\bar{I}(j,k)$. Like for the z coordinate calculation, the x position is sampled in a small neighborhood with a typical size of 7×3 or 9×4. The mean value of $\bar{I}(j,k)$ sampled in the specified neighborhood is then taken as the x coordinate of the control point. The voxels used in the determination of the x coordinate (for y as well, because the phantom is symmetrical with respect to the x and y axes) form a volume and is referred to as PSV(xy). The placement of PSV(xy) is similar to that for PSV(z), but needs to be within the frame of the grid. For the determination of the y coordinate, the procedure is exactly the same by using the first derivative calculated along the y axis. The first moment $\bar{J}(i,k)$

$$\bar{J}(i,k) = \frac{\sum_{p=1}^{n_y} j_p |g^y(i,j_p,k)|}{\sum_{p=1}^{n_y} |g^y(i,j_p,k)|} \tag{3}$$

is used for the determination of the y coordinate. n_y is the number of voxels used in the evaluation of the first moment and $|g^y(i, j, k)|$ is the magnitude of the first derivative along the y axis [see Eq. (A3)].

In the present work, a laboratory-based coordinate system is used for the positions of the control points measured in Euclidean coordinates. This coordinate axis system has its origin at the isocentre of the scanner, which is also taken to be the isocentre of the gradient field generating devices. Its x axis is taken to be along the left/right direction, the y axis along the anterior/superior direction, and the z axis along the head/foot direction. The geometric distortion can then be characterized by the differences in the coordinates of the control points

$$\begin{aligned} dx_p &= x'_p - x_p \\ dy_p &= y'_p - y_p \\ dz_p &= z'_p - z_p \\ dr_p &= \sqrt{(dx_p)^2 + (dy_p)^2 + (dz_p)^2} \\ (p &= 1, 2 \ldots .N) \end{aligned} \tag{4}$$

Here, x'_p, y'_p and z'_p are the coordinates of the control point p measured in the distorted image space; x_p, y_p and z_p are the corresponding coordinates measured in the undistorted physical space of the phantom, and N is the total number of control points. It is due to this one-to-one correspondence that a detailed mapping of geometric distortion is obtained.

4. Correction of image geometric distortion

Following mapping of the geometric distortion arising from an accurate knowledge of the positions of the control points, the correction of the distortion simply becomes a problem of interpolation. This interpolation can be symbolically expressed as

$$\begin{pmatrix} x' \\ y' \\ z' \end{pmatrix} = \mathcal{P} \begin{pmatrix} x \\ y \\ z \end{pmatrix} \tag{5}$$

where x, y and z are the coordinates of any given spatial point in the undistorted physical space; x', y' and z' are the coordinates of its corresponding point in the distorted image space, and $\mathcal{P}$ represents an interpolation model through which this correspondence is established. The transformation expressed by Eq. (5) is also referred to as spatial transformation.

There are two general approaches to spatial transformations: global transformation and piecewise interpolation. Global transformations, such as the polynomial transformations used in some previous studies [2,11], impose a single mapping function upon the entire imaging volume of interest. In that approach, the use of a single function sometimes cannot adequately account for local geometric distortions. In order to manage local distortions, piecewise mapping has

been introduced [14,15]. Because the primary aim of the present work is to provide a comprehensive and accurate mapping of the geometric distortion, piecewise interpolations have been adopted.

For piecewise interpolation, a range of models are available. These models, however, were developed mainly to deal with two-dimensional problems. Although some models can be easily extended to 3D, one problem associated with this extension, particularly for the present work with a significantly large number of data points, is the exponential increase in computational time. A detailed study of the various interpolation models will be presented in a separate publication. It was found, however, that trilinear interpolation, the simplest interpolation of all, performed as satisfactorily as more sophisticated interpolation models. In order to complete the correction process, a second interpolation is required for interpolating the image intensity. Again, the trilinear interpolation was used.

5. Assessment of the method

The method has been tested on three separately acquired image data sets. The images were acquired with a Siemens Sonata 1.5T MRI scanner located at a local hospital. The phantom was positioned at the magnet isocentre and imaging was performed using a body coil. An inversion recovery gradient echo 3D imaging sequence was used with following imaging parameters: TR (repetition time) = 1540 ms; TE (echo time) = 1.53 ms; TI (inversion time) = 1100 ms; imaging array size = 256 × 256 × 256; FOV (field-of-view) = 334.0 mm × 334.0 mm × 307.2 mm. The corresponding voxel's dimensions were 1.305 mm × 1.305 mm × 1.200 mm. Because of the relatively low sensitivity of the body coil, multiple acquisitions were used. Three image data sets were acquired in a single session with the phantom's position unaltered. The first two data sets (data sets 1 and 2) were acquired with four acquisitions each and were acquired one after the other. The third data set (data set 3) was then acquired with eight acquisitions. In the acquired images, as some slices at the phantom edges contained serious image artifacts, only the control points defined by the central part of the array, 19 × 19 × 25 with a total of 9025 control points, were used in the assessment studies of the method. Precision positioning of the phantom in the scanner was enabled using scanner's laser positioning facility.

The reproducibility of the method was tested by comparing the measured positions of the control points between the three repeatedly acquired data sets. The test also included a study of the differences in the measured positions by using different PSV sizes. For the estimation of the accuracy, it needs to be acknowledged that the measurement of the accuracy can be extremely difficult if it is not impossible. Manual identification relying on human vision is sometimes regarded as an "accurate" method, but such a claim has always been questioned due to the subjective variability involved. Manual identification is also impractical for the present work, as the number of the control points in the phantom is large. Moreover, the accuracy in manual identification is limited as it does not provide accuracy at a sub-pixel (or sub-voxel) level. Because of these limitations the following method was used to provide an alternative for accuracy assessment. Accuracy was assessed by estimating the measured residual geometric distortions in the corrected images. If the positions of the control points have been measured accurately, the corrected images can then be expected to contain little or no geometric distortion. Any residual distortion measured in the corrected images can then be used as an overall measure of the accuracy. This method has also been used by previous investigators [11].

6. Results

In the top row of Fig. 9, representative transverse slices of uncorrected phantom images are shown. Geometric distortions are clearly visible in these images. The distortion increases as the distance from the magnet isocentre increases. For example, in the slice shown in the top right corner of Fig 9, which is at $z = 110$ mm, the grids shown in the central region and those in the corner areas were actually from two neighboring grid sheets. In the bottom row, representative slices of the corrected images are shown. By visual inspection, the corrected images showed no noticeable geometric distortion. More quantitative analysis relating to the geometric distortion is presented in Fig. 10. Here, samples of geometric distortion selected in certain planes by calculating the errors in the coordinates between the image positions and the true positions [Eq. (4)] are shown. Large errors are present in the uncorrected images. Maximum errors were over 9.00 mm. For comparison, samples of the errors measured in the corrected images are given in Fig. 11. It is clearly demonstrated here that in the corrected images the errors were negligible. The maximum errors were ~0.6 mm.

Representative quantitative results on reproducibility and accuracy are presented in Tables 1–3. In Table 1, statistical data for the absolute differences in the measured coordinates of the control points compared between three repeated data sets are tabulated. The means errors in the absolute differences in the coordinates (x, y, and z) and in the positional displacement (r) were only ~0.1 mm or less, indicating an excellent reproducibility. The standard deviations were also very small. Also included is the maximum absolute difference. There is no single control point whose absolute difference in the coordinates (x, y and z) or in its positional displacement (r) exceeded 0.7 mm. In Table 2, representative statistical data on the differences in the coordinates obtained using two different sets of PSVs are presented, showing an extremely high level of reproducibility. Both the means and standard deviations were in the

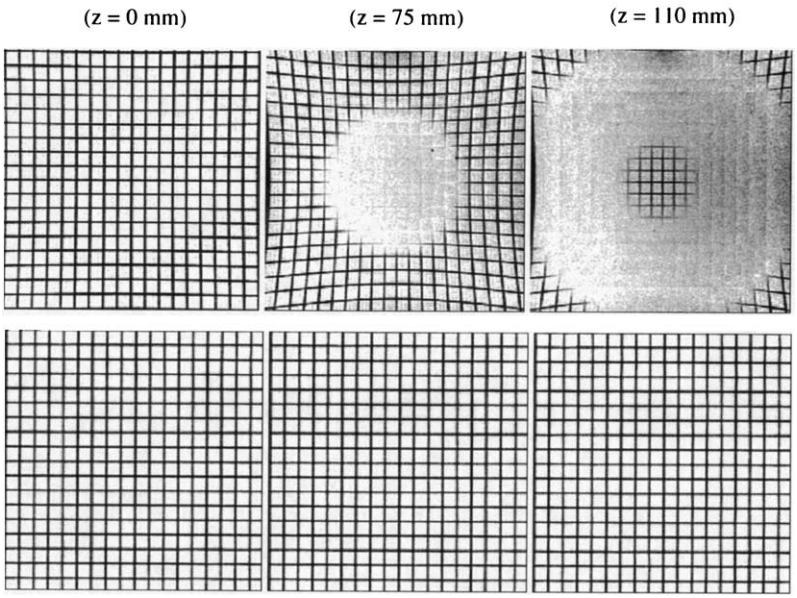

Fig. 9. Representative transverse slices of the phantom image selected at different locations before correction (top row); and three slices selected at similar locations after correction (bottom row).

order of 0.1 mm. All maximum absolute differences were less than 0.5 mm.

The representative results for the accuracy assessment are summarized in Table 3. Here, the differences in the coordinates of the control points between those measured from the phantom images (uncorrected and corrected) and that measured from the known dimensions of the phantom are tabulated. Before the correction, the mean absolute differences in the coordinates were about 1.4 mm and in the positional displacement 2.8 mm. The maximum differences were found to vary between 6.9 mm and 9.5 mm for the coordinates and exceeded 10.0 mm for the positional displacement. After correction, the mean absolute differences in the coordinates were ~0.1 mm or less. The mean absolute differences in the positional displacement were slightly larger, between 0.17 mm and 0.21 mm. The standard deviations were 0.10 or less. The maximum absolute differences were ~0.6 mm.

7. Discussion

As pointed out in the Introduction, for a comprehensive and accurate three-dimensional mapping of the geometric distortion, the two key requirements are a dense distribution of the control points and a robust and accurate method for the positional measurement of these control points. These two key requirements have clearly been met in the present method and the success is reflected by the accuracy of the method. The central concept used in the present method is to use a phantom that provides three orthogonal planes to define a point in space. Phantoms using this design approach easily allow as many control points as desired, and the number of control points is limited only by necessity. The 3D phantom described in this article contained an array of 10,830 control points (although only 9025 were used in the assessment study) in a field of view 257.0 mm × 259.0 mm × 261.0 mm. By simply changing the grid dimensions and the width of the grid sheets, phantoms with any desired density of the array points (the control points) can be easily constructed. To improve the procedure grid sheets with grid dimensions of 10.0 mm × 10.0 mm and 10.0 mm in sheet thickness are being resourced. With such grids, a phantom with the array dimensions of 260.0 mm × 260.0 mm × 260.0 mm will have a total of 19,683 control points.

An important aspect of the success of the method is clearly the high accuracy in the positional measurements of the control points (see Table 3). The mean errors in the measured coordinates of the control points with the present method were in the order of 0.1 mm. The maximum errors were ~0.6 mm. These errors are small, considering the extent of the distortions in the original phantom images (see Figs. 9 and 10 and Table 3). Even greater accuracy can be achieved for mapping geometric distortion with a head coil. (With head coils, phantom images with smaller voxel sizes and better signal-to-noise ratios can be generated. With smaller voxels, the edges that define the interfacial boundaries become sharper and the positions of the planes can be more accurately measured).

The reproducibility data have shown that the method is extremely robust. The measured coordinates of the control points either in repeated image data sets or with differently selected PSV sizes all showed a high level of reproducibility (see Tables 1 and 2). The mean errors were very small, between 0.02 and 0.12 mm. The standard deviations were also negligibly small. The maximum errors were ~0.6 mm. It should be noted that this high level of robustness was

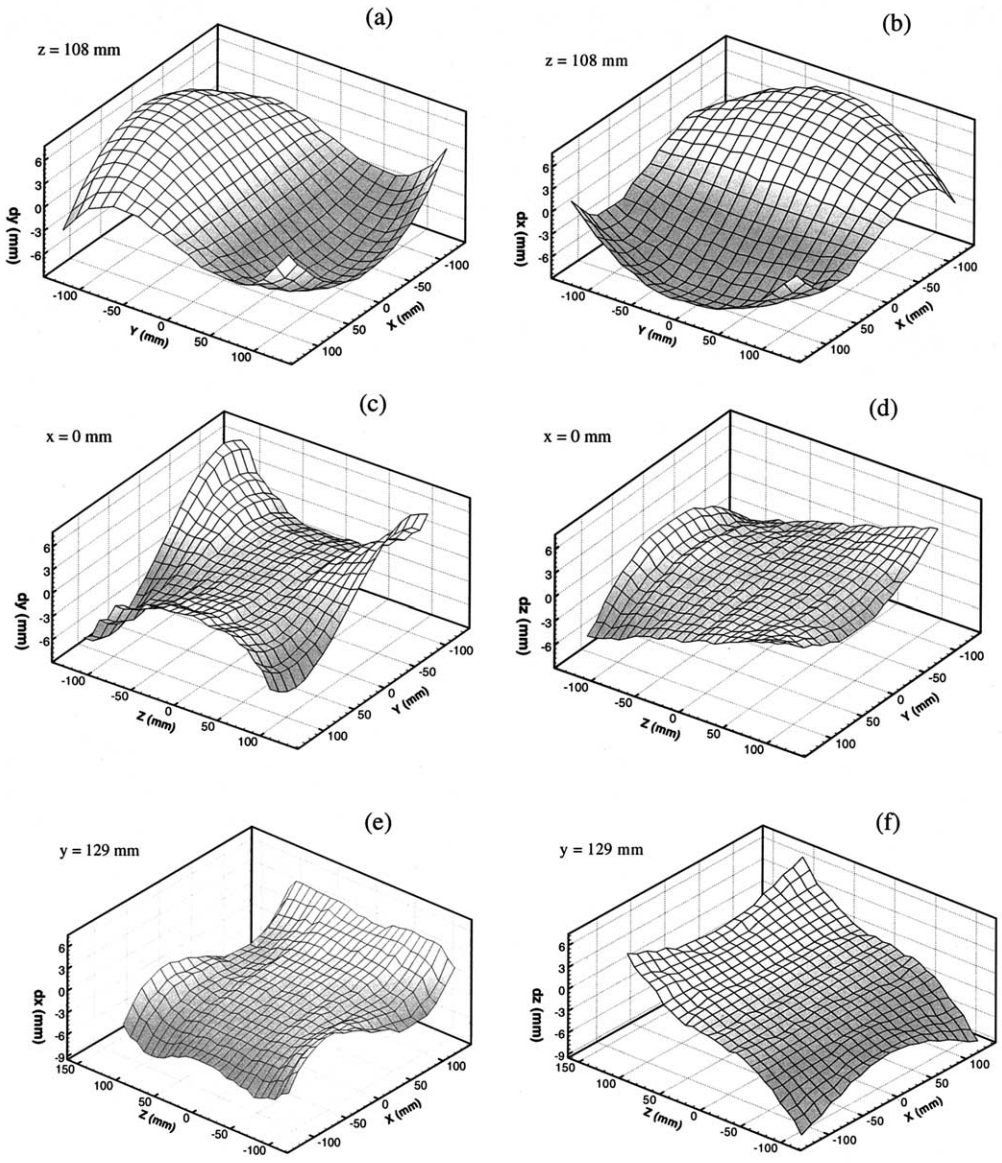

Fig. 10. (a) to (f) Samples of the measured geometric distortion in certain planes at different locations.

achieved on the phantom images with relatively low quality. For the three data sets used, the mean signal-to-noise ratio (SNR) was only 13.6 in data set 1, 13.7 in data set 2, and 19.4 in data set 3 (this data set was acquired with twice the number of acquisitions). In addition, SNR showed large spatial variations in the imaging volume and in some regions, SNR dropped to ~5.0. Also, it was noticed that the intensity of the phantom images was highly inhomogeneous. Although a number of factors might have contributed to the robustness of the method, the most important factor is believed to be the use of the 3D Prewitt operators. These operators inherently have an effective smoothing capability that allowed an accurate estimation of the control points. It also should be noted that the method is entirely automated. There are no steps in which subjective decisions are required.

The method described herein has a number of quantifiable advantages to that described in [11]. First, the number of control points in the present method can be made as large as desired, whereas in the sphere-based approach, the number of control points is limited. The phantom described in the present work had 10,830 control points compared to 792 in a phantom of similar size that used spheres [11]. Secondly, the present method is more accurate. If the maximum absolute difference in the positional displacement is used as a measure, the present method reduced it from over 10.00 mm before the correction to ~0.6 mm after the correction, a reduction by a factor of more than 15. By comparison, using the method described in [11], the reduction was about fourfold from 4.3 mm before the correction to ~1.0 mm after the correction. A similar performance difference was also observed in the reduction in the mean errors of the

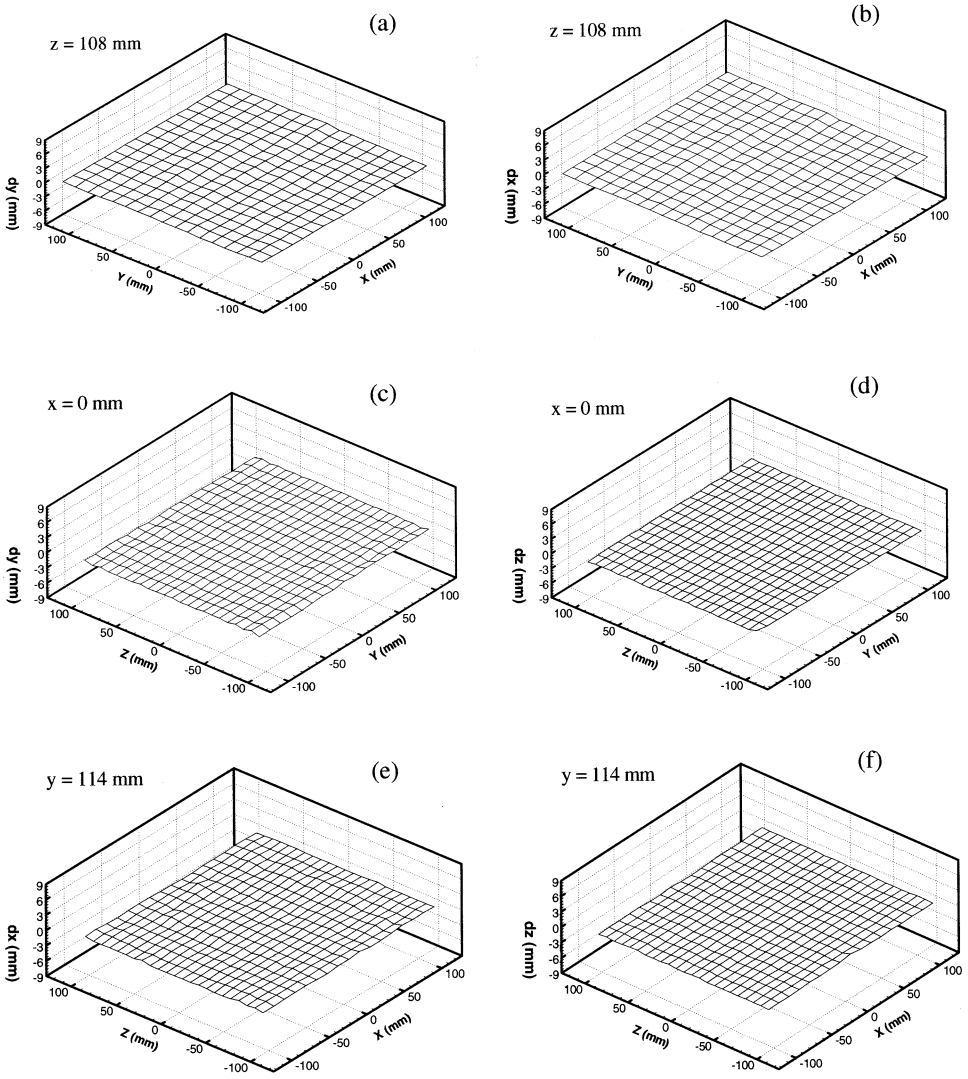

Fig. 11. (a) to (f) Samples of the measured residual geometric distortion in the corrected images in certain planes at different locations.

positions of the control points between the two methods. Thirdly, the present design of the phantom is extremely simple and flexible. In addition, the collection of the phantom MR images needed to map the geometric distortion is also simple.

Any local deformation should not significantly affect the accuracy in the measurement of the positions of the control points, as the positions of the planes for each control point are determined only in a small neighborhood, typically 5 to 7 voxels along each direction. On such relatively small scales, any deformations of the planes should be negligibly small and, therefore, the effect due to the deformations should also be small.

8. Conclusion and the potential impact

The 3D phantom and the method that has been developed specifically for the positional measurement of the control

Table 1
Summary of the statistical data (μ, σ, *max*) of the absolute errors in the measured coordinates of the control points compared between the three different data sets described in the text

Data set I	Data set II	Direction	μ (*mm*)	σ	*max* (*mm*)
1	2	*x*	0.06	0.06	0.53
		y	0.05	0.04	0.40
		z	0.06	0.05	0.48
		r	0.11	0.06	0.70
1	3		0.05	0.05	0.52
			0.04	0.04	0.40
			0.05	0.04	0.40
			0.10	0.06	0.61
2	3		0.05	0.05	0.53
			0.04	0.04	0.37
			0.05	0.04	0.54
			0.10	0.06	0.60

The PSV sizes used were: PSV(xy) = 7 × 7 × 3 and PSV(z) = 3 × 3 × 5.

Table 2
Summary of the statistical data (μ, σ, *max*) of absolute errors in the measured coordinates of the control points obtained with different sizes of PSVs

Data set	PSV size (Set I)	PSV size (Set II)	Direction	μ (*mm*)	σ	*max* (*mm*)
1	$7 \times 7 \times 3$	$9 \times 9 \times 4$	x	0.05	0.04	0.27
	PSV (xy)	PSV (xy)	y	0.02	0.02	0.13
	$3 \times 3 \times 5$	$5 \times 5 \times 7$	z	0.09	0.07	0.46
	PSV (z)	PSV (z)	r	0.12	0.07	0.46
2				0.05	0.04	0.27
				0.02	0.02	0.16
				0.09	0.07	0.45
				0.12	0.07	0.45
3				0.05	0.04	0.27
				0.02	0.01	0.10
				0.10	0.08	0.44
				0.12	0.07	0.44

points in the phantom described in this article have been demonstrated to be capable of providing a comprehensive, 3D mapping of geometric distortion inherent in MRI images. A novel approach using three orthogonal planes to define control points in 3D space was employed in this method. This novel design of the phantom easily allows as many control points as desired. In summary, the mean errors in the measured coordinates of the control points were typically ~0.1 mm, which were less than one tenth of the voxel dimensions of the phantom images. Moreover, the maximum absolute errors were only ~0.6 mm, reduced from over 10.0 mm in the original uncorrected images (see Table 3).

Table 3
Summary of the statistical data (μ, σ, *max*) of the differences (absolute) between the measured coordinates of the control points in the phantom images (uncorrected or corrected) and the corresponding coordinates measured directly from the physical dimensions of the phantom

Data set	Status	Direction	μ (*mm*)	σ	*max* (*mm*)
1	uncorrected	x	1.46	1.47	8.12
		y	1.44	1.39	6.90
		z	1.36	1.35	9.50
		r	2.83	2.00	10.67
1	Corrected		0.08	0.07	0.53
			0.09	0.07	0.52
			0.07	0.07	0.58
			0.17	0.08	0.60
2	Uncorrected		1.46	1.47	8.09
			1.44	1.39	7.02
			1.36	1.35	9.31
			2.83	1.99	10.54
2	Corrected		0.09	0.08	0.60
			0.10	0.08	0.60
			0.10	0.08	0.56
			0.20	0.09	0.64
3	Uncorrected		1.46	1.47	8.14
			1.44	1.39	7.03
			1.36	1.35	9.33
			2.83	1.99	10.56
3	Corrected		0.08	0.07	0.58
			0.11	0.09	0.58
			0.11	0.10	0.50
			0.21	0.10	0.68

The simplicity, accuracy and effectiveness in mapping the geometric distortion demonstrated in the present method may indicate that the method can have some impact on those areas of MRI requiring accurate and reproducible imaging. For example, the 3D phantom can be used to provide a comprehensive quality assurance program for geometric distortion that can never be achieved with any phantoms designed for 2D measurements. There is no doubt that the accurately mapped geometric distortion obtained with the method can be used to improve the accuracy and sensitivity both in structural and functional MRI. The method may have potential to make MRI a stand-alone imaging modality in applications where geometric accuracy is highly demanded, such as in radiosurgery and radiotherapy. Importantly, the method can also provide an effective way for image quality control in large-scale longitudinal studies using MRI.

Acknowledgments

We would like to express our thanks to the staff at our workshop for the construction of the phantom, and to Liu Feng and Daniel Barnes for helping with preparation of the figures.

Appendix: The 3D Prewitt operators

Prewitt operators were initially introduced in 2D to provide an approximation for the first derivatives [13]. These operators can be viewed as a discrete evaluation of the first derivatives. The 2D Prewitt operators are defined by a set of 3×3 masks. For example, the mask that is used for an approximate first derivative along the $+x$ axis (the horizontal axis of the image) is

$$\begin{bmatrix} -1 & 0 & 1 \\ -1 & 0 & 1 \\ -1 & 0 & 1 \end{bmatrix}$$

The convolution of this mask with a two-dimensional image will provide an approximation for the first derivative along the $+x$ axis for every pixel in the image, except for those pixels on the image boundaries for which the Prewitt operators are not applicable. The explicit calculation involved in the convolution process is

$$\begin{aligned} g^x(i,j) = {} & f(i+1, j-1) - f(i-1, j-1) \\ & + f(i+1, j) - f(i-1, j) \\ & + f(i+1, j+1) - f(i-1, j+1) \end{aligned} \tag{A1}$$

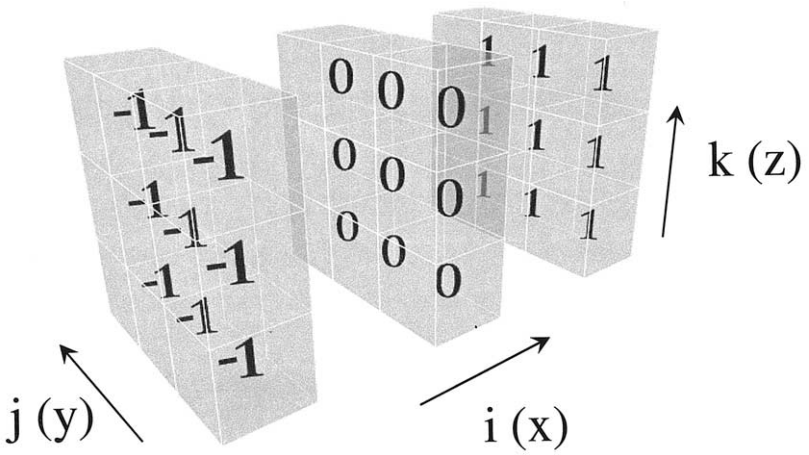

Fig. A1. The mask used in the 3D Prewitt operator that provides an approximation for the first derivative along the x axis (i direction) as indicated.

where $g^x(i, j)$ denotes the approximate first derivative along the $+x$ axis for the pixel at (i, j) and f is the image function (gray scale intensity). A scaling factor of 1/3 is often used to normalize the first derivatives.

The 2D Prewitt operators can be extended to provide an approximation for the first derivatives in 3D. The 3D equivalents of the 2D Prewitt operators are defined by a set of 3 × 3 × 3 masks. Each of these masks contains 26 neighboring voxels in 3D. For convenience, these operators are referred to as 3D Prewitt operators. In the present work only the 3D Prewitt operators that provide approximate values of the first derivative along the three principal axes, x, y and z axes (or, i, j, and k directions) are introduced.

The 3D Prewitt operator that provides an approximate value for the first derivative along the $+x$ axis uses the mask as shown in Fig. A1. The explicit calculation involved in the convolution process is

$$\begin{aligned} g^x(i,j,k) &= f(i+1,j-1,k-1) - f(i-1,j \\ &- 1,k-1) + f(i+1,j-1,k) - f(i \\ &- 1,j-1,k) + f(i+1,j-1,k+1) \\ &- f(i-1,j-1,k+1) + f(i+1,j,k \\ &- 1) - f(i-1,j,k-1) + f(i \\ &+ 1,j,k) - f(i-1,j,k) + f(i+1,j,k \\ &+ 1) - f(i-1,j,k+1) + f(i+1,j \\ &+ 1,k-1) - f(i-1,j+1,k-1) \\ &+ f(i+1,j+1,k) - f(i-1,j+1,k) \\ &+ f(i+1,j+1,k+1) - f(i-1,j \\ &+ 1,k+1)(A2) \end{aligned} \tag{A2}$$

where $g^x(i, j, k)$ is the approximate value for the first derivative for the voxel at (i, j, k), and f is the image function in 3D. The first derivative is approximated by averaging the differences of the gray scale intensities between nine pairs of the neighboring voxels. By simply rotating the axes, masks can be easily defined for the two operators that provide approximate values for the first derivatives along the y and z axes. The calculations involved in the corresponding convolution processes are

$$\begin{aligned} g^y(i,j,k) &= f(i-1,j+1,k-1) \\ &- f(i-1,j-1,k-1) + f(i-1,j+1,k) \\ &- f(i-1,j-1,k) + f(i-1,j+1,k+1) \\ &- f(i-1,j-1,k+1) + f(i,j+1,k-1) \\ &- f(i,j-1,k-1) + f(i,j+1,k) - f(i,j-1,k) \\ &+ f(i,j+1,k+1) - f(i,j-1,k+1) \\ &+ f(i+1,j+1,k-1) - f(i+1,j-1,k-1) \\ &+ f(i+1,j+1,k) - f(i+1,j-1,k) \\ &+ f(i+1,j+1,k+1) \\ &- f(i+1,j-1,k+1) \end{aligned} \tag{A3}$$

and

$$\begin{aligned} g^z(i,j,k) &= f(i-1,j-1,k+1) \\ &- f(i-1,j-1,k-1) + f(i-1,j,k+1) \\ &- f(i-1,j,k-1) + f(i-1,j+1,k+1) \\ &- f(i-1,jf(i-1,j+1,k-1) \\ &+ f(i,j-1,k+1) - f(i,j-1,k-1) \\ &+ f(i,j,k+1) - f(i,j,k-1) + f(i,j+1,k+1) \\ &- f(i,j+1,k-1) + f(i+1,j-1,k+1) \\ &- f(i+1,j-1,k-1) + f(i+1,j,k+1) \\ &- f(i+1,j,k-1) + f(i+1,j+1,k+1) \\ &- f(i+1,j+1,k-1) \end{aligned} \tag{A4}$$

where g^y *(i, j, k)* and g^z *(i, j, k)* are the approximate values for the first derivatives along the *y* and *z* axes.

References

[1] Price RR, Axel L, Morgan T, et al. Quality assurance methods and phantoms for magnetic resonance imaging: report of AAPM nuclear magnetic resonance Task Group No. 1. Med Phys 1990;17:287–95.
[2] Kawanaka A, Takagi M. Estimation of static magnetic field and gradient fields from NMR image. J Phys [E] 1986;19:871–5.
[3] Mizowaki T, Nagata Y, Okajima K, et al. Reproducibility of geometric distortion in magnetic resonance imaging based on phantom studies. Radiother Oncol 2000;57:237–42.
[4] Walton L, Hampshire A, Forster DMC, Kemeny AA. A phantom study to assess the accuracy of stereotactic localization, using T1-weighted magnetic resonance imaging with the Leksell stereotactic system. Neurosurgery 1996;38:170–8.
[5] Walton L, Hampshire A, Forster DMC, Kemeny AA. Stereotactic localization with magnetic resonance imaging: a phantom study to compare the accuracy obtained using two-dimensional and three-dimensional data acquisitions. Neurosurgery 1997;41:131–9.
[6] Yu C, Apuzzo MLJ, Zee CS, Petrovich Z. A phantom study of the geometric accuracy of computed tomographic and magnetic resonance imaging stereostatic localization with the Leksell stereostatic system. Neurosurgery 2001;48:1092–9.
[7] Sumanaweera TS, Glover G, Song S, Adler JR, Napel S. Quantifying MRI geometric distortion in tissue. Magn Reson Med 1994;31:40–7.
[8] Orth RC, Sinha P, Madsen EL, et al. Development of a unique phantom to assess the geometric accuracy of magnetic resonance imaging for stereotactic localization. Neurosurgery 1999;45:1423–31.
[9] McRobbie DW. A three-dimensional volumetric test object for geometric evaluation in magnetic resonance imaging. Med Phys 1997; 24:737–42.
[10] Lerski RA, de Wilde J, Boyce D, Ridgeway J. Quality control in magnetic resonance imaging, IPEM Report 80. York: The Institute of Physics and Engineering in Medicine, 1998.
[11] Breeuwer M, Holden M, Zylka W. Detection and correction of geometric distortion in 3D MR images. Proc SPIE 2001;4322:1110–20.
[12] Holden M, Breeuwer M, Mcleish K, Hawkes DJ, Keevil SF, Hill DLG. Sources and correction of higher order geometrical distortion for serial MR brain imaging. Proc SPIE 2001;4322:69–78.
[13] Sonka M, Hlavac V, Boyle R. Image processing, analysis and machine vision. Cincinnati: International Thomson Publishing Inc, 1996.
[14] Franke R. Scattered data interpolation: tests of some methods. Math Comput 1982;38:181–200.
[15] Hardy RL. Multi-quadratic equations of topography and other irregular surfaces. J Geophys Res 1975;10:321–32.